AIAA 2004-0659

Validation Study of a Multidomain Spectral Element Code for Simulation of Turbulent Flows*

G.B. Jacobs†
Brown University
Providence, RI, 02912

D.A. Kopriva‡
Florida State University
Tallahassee, FL 32306

F. Mashayek§
University of Illinois at Chicago
Chicago, IL 60607

Abstract

We present a validation study of a Chebyshev multidomain staggered-grid method[1] (CMSM) for numerical simulation of three-dimensional compressible turbulent flows. Computations with CMSM of an isotropic turbulence and a fully-developed turbulent channel flow are compared with previously published results. Turbulence initiation issues are discussed and resolution requirements are assessed at a minimum of three to six points per wave number for a polynomial approximation of ten to thirteen.

Nomenclature

C_p	specific heat
e	energy flux
$E(k)$	energy spectrum
F, G, H	flux vector in x, y and z directions
h_j	Lagrangian polynomial on Gauss grid
$\mathbf{i}$	the complex number $\sqrt{-1}$
J	Jacobian
k	wave number
l_j	Lagrangian polynomial on Lobatto grid
L	non-dimensional length
L_f	reference length
M_f	$U_f/\sqrt{\gamma R T_f}$ reference Mach number
Ma	$u_{ctr} M_f/\sqrt{T}$ Mach number
N	number of grid points per subdomain in each directions
p	$\rho T/\gamma M_f^2$ pressure
$\mathbf{P}_N$	Space of polynomials of degree less than or equal to N
Pr	$C_p \mu/\kappa$ Prandtl number
$\wp$	approximation order
Q	vector of solution unknowns
R	gas constant
Re_f	$\rho_f U_f L_f/\mu$ reference Reynolds number
t	time
T	temperature
u, v, w	velocity in x, y and z directions
u_τ	skin friction velocity
U_f	reference velocity
x, y, z	spatial coordinate in x, y and z directions
X, Y, Z	spatial coordinate in X, Y and Z directions in mapped space

Greek symbols

γ	ratio of the specific heats
ϵ	turbulence dissipation
κ	thermal conductivity
μ	viscosity
ρ	density
τ	shear stress
ϕ	uniformly random generated number
ω	vorticity

Subscripts

d	dillatational
rms	root mean square
s	solenoidal
t	derivative with respect to t
x, y, z	derivative with respect to x, y and z
X, Y, Z	derivative with respect to X, Y and Z

Superscripts

a	advective flux

†Visiting Assistant Professor, Division of Applied Mathematics

‡Professor, Department of Mathematics

§Associate Professor, Department of Mechanical Engineering, Associate Fellow of AIAA.

v	viscous flux
$\vec{}$	vector
$\check{}$	mapped space variable
$\tilde{}$	Favre averaged property
$\bar{}$	Reynolds averaged property
$'$	Reynolds fluctuating property
$''$	Favre fluctuating property
$+$	normalized with wall coordinate

Introduction

In the last two decades direct numerical simulation (DNS) has become a viable research tool for the study of low and moderate Reynolds number turbulent flows. It has helped increase the physical understanding of various flows. DNS results has also supplied a large database for model development and validation.

At first sight, DNS appears to be a simple procedure since the Navier-Stokes equations are discretized directly without the use of turbulence models. However, the turbulence at Reynolds numbers that are relevant to engineering applications has a large range of scales. This means that computation of such flows with a standard low-order CFD scheme, whose errors are typically dominated by large dispersion an dissipation errors, would require an unrealistically large number of grid points.

To reduce the problem size, high-order methods that can resolve small scales efficiently are needed for DNS. The research efforts into these kinds of methods are numerous (see e.g. Moin and Mahesh[2] for a review), and involve many related issues such as treatment of boundary conditions, iteration schemes and multidomain methods. In our ongoing research effort[3,4] we are developing a Chebyshev multidomain spectral method (CMSM)[1] for DNS. It is spectrally accurate, has low dispersion and it can deal with complex geometries.

In this paper we asses resolution requirements and discuss initialization issues for benchmark simulations of isotropic decaying turbulence and the turbulent flow in a channel with CMSM.

In the remainder of this paper, we first present the governing equations and discuss the numerical methodology. Then, initialization of the isotropic turbulence for CMSM is presented, followed by a comparison of results between CMSM simulations and simulations with a Fourier spectral method presented in Blaisdell *et al.*[5] Then the channel flow initialization is discussed, followed by a comparison of the results between CMSM simulations and simulations in Moser *et al.*[6] with a spectral method.

Governing Equations

We consider a compressible and Newtonian fluid with zero bulk viscosity that obeys the perfect gas equation of state. The Navier-Stokes equations in dimensionless, conservation form for the fluid are

$$\vec{Q}_t + \vec{F}^a_x + \vec{G}^a_y + \vec{H}^a_z = \frac{1}{Re_f}(\vec{F}^v_x + \vec{G}^v_y + \vec{H}^v_z). \qquad (1)$$

The equations for $\vec{Q} = [\rho, \rho u, \rho v, \rho w, \rho e]$ represent conservation of mass, momentum (in three directions) and energy, respectively. F, G, and H represent the advective (superscript 'a') and viscous (superscript 'v') fluxes in three directions. $\rho e = \frac{p}{\gamma-1} + \rho(u^2+v^2+w^2)/2$ is the sum of the internal and kinetic energy. The equation of state is $p = \rho T/\gamma M_f^2$. All of the variables are normalized by reference length (L_f), density (ρ_f), velocity (U_f), and temperature (T_f) scales. The reference Reynolds, Mach and Prandtl numbers are defined by $Re_f = \rho_f U_f L_f/\mu$, $M_f = U_f/(\gamma R T_f)^{1/2}$ and $Pr = C_p\mu/\kappa$, respectively.

Numerical Methodology

The computational methodology is described in detail in Refs. 1 and 7; this section provides a summary. The approximation begins with the subdivision of the region under consideration into non-overlapping quadrilateral subdomains, or elements. Each element is then mapped onto a unit square by an isoparametric transformation using the linear blending formula. Under the mappings, (1) becomes

$$\check{Q}_t + \check{F}_X + \check{G}_Y + \check{H}_Y = 0, \qquad (2)$$

where

$$\begin{aligned} \check{Q} &= J\vec{Q}, \\ \check{F} &= X_x\vec{F} + X_y\vec{G} + X_z\vec{H}, \\ \check{G} &= Y_x\vec{F} + Y_y\vec{G} + Y_z\vec{H}, \\ \check{H} &= Z_x\vec{F} + Z_y\vec{G} + Z_z\vec{H}. \end{aligned} \qquad (3)$$

Within an element the solution values, $\check{Q}$, and the fluxes $\check{F}$, $\check{G}$ and $\check{H}$ in (2) are approximated on separate grids. These grids are tensor products of the Lobatto grid, X_j, and the Gauss grid, $X_{j+1/2}$, mapped onto $[0,1]$:

$$\begin{aligned} X_j &= \tfrac{1}{2}\left(1-\cos\left(\tfrac{j}{N}\pi\right)\right) \quad j = 0,1,\ldots,N, \\ X_{j+1/2} &= \tfrac{1}{2}\left(1-\cos\left(\tfrac{2j+1}{N}\pi\right)\right) \quad j = 0,1,\ldots,N-1. \end{aligned} \qquad (4)$$

On these grids the Lagrange interpolating polynomials $l_j(\xi) \in \mathbf{P}_N$ and $h_{j+1/2}(\xi) \in \mathbf{P}_{N-1}$ are defined. Together with the choice of collocation points in equation (4), these polynomials represent a Chebyshev approximation on each grid. The motivation for the staggered grid is that polynomial approximations of degree N that are to be differentiated once are represented on a Lobatto grid. Other quantities are of degree $N-1$, and are represented on a Gauss grid.

Thus solution unknowns are collocated at Gauss points while fluxes are collocated at Lobatto points. The solution is denoted by:

$$\check{Q}(X,Y,Z) = \sum_{i=0}^{N-1}\sum_{j=0}^{N-1}\sum_{k=0}^{N-1} Q_{i+1/2,j+1/2,k+1/2} \; h_{i+1/2}(X)h_{j+1/2}(Y)h_{k+1/2}(Z). \quad (5)$$

¿From this polynomial, the solution values are computed at the Lobatto points. Although the solutions at the Lobatto points still describe a polynomial in $\mathbf{P}_{N-1}$, application of boundary and interface conditions add the extra degree of freedom to increase the polynomial order.

The inviscid fluxes are determined by evaluating the interpolant from (5) at the desired Lobatto and Lobatto points. At points interior to the element, the fluxes are computed directly. Along element faces, a Roe solver[8] is used to compute the flux using two solutions from the current and neighboring elements.

The computation of the viscous flux uses a two-step procedure. Since the reconstruction of the solution from the Gauss points onto the Lobatto points gives a discontinuous solution at the element faces, it is necessary to construct first a continuous piecewise polynomial approximation before differentiating. To construct the continuous approximation, the average of the solutions on either side of the interface is used as the interface value. The continuous solution is then differentiated to get the derivative quantities needed for the viscous fluxes. Since differentiation reduces the polynomial order by one, it is natural then to evaluate the differentiated quantities on the Gauss grid. Once the derivative quantities are evaluated at the Gauss points, a polynomial interpolant of the form (5) is defined, so that the gradients can be evaluated at the Lobatto points. From the cell face values, the viscous flux are computed and combined with the inviscid fluxes to obtain the total flux.

Note that evaluating the gradients at the cell centers has two desired effects. First, it makes the evaluation of the divergence consistent with that used in the continuity equation. Second, the evaluation of the viscous fluxes will not require the use of subdomain corner points.

Boundary Conditions

Since only an isothermal wall boundary condition is used for simulation in this paper, we will restrict our discussion to this boundary condition treatment.

Isothermal wall boundaries. At solid wall boundaries, no-slip conditions are imposed for the velocity and an isothermal condition for the temperature. As before, the computations of the viscous and inviscid fluxes are treated separately. The no-slip condition is enforced on the inviscid flux by imposing a flow on the other side of the wall with equal but opposite velocity. Since the wall is isothermal, the internal energy is set using the wall boundary temperature. Thus, if the evaluation of (5) at a vertical wall point $(X_0, Y_{j+1/2})$ gives $\vec{Q}_{0,j+1/2} = [\rho, \rho u, \rho v, \rho e]^T_{0,j+1/2}$ the external state $\vec{Q}_e = [\rho, -\rho u, -\rho v, \rho e]^T$ is defined, where $\rho e_{0,j+1/2}$ is given by $\rho T_{wall}/[\gamma(\gamma-1)M_f^2] + [(\rho u)^2 + (\rho v)^2]/2\rho$. The advective flux is then determined with an Osher solver. The viscous flux at a wall is computed in two stages, as described above. After the solution is reconstructed at the cell faces, the Dirichlet conditions $\rho u_{0,j+1/2} = \rho v_{0,j+1/2} = 0$ are set. If the wall is isothermal, then $T_{0,j+1/2} = T_{wall}$ is set. After the quantities ∇u, ∇v, ∇T are interpolated back onto the faces, the viscous flux is added to the advective flux to obtain the total flux.

Isotropic turbulence

In this section we repeat a simulation of isotropic decaying turbulence that was performed in Ref. 5 with a Fourier pseudo-spectral method. The purpose is twofold. Firstly, it provides a rigorous code testing for the simulation of compressible turbulence with CMSM. Secondly, an indication of resolution requirements for DNS of turbulent flow is obtained through comparison with the results of the well-established Fourier spectral method.

Initial Conditions

The simulation of isotropic turbulence is performed in a cube with periodic boundary conditions, which eliminates issues involved in specifying boundary conditions. The absence of specified boundary conditions, however, introduces the problem of generating turbulence, since no turbulent fluctuations can be specified at an inflow boundary. In addition, the simulation of decaying turbulence by definition lacks the presence of a source term that could generate turbulence.

Rogallo,[9] Blaisdell *et al.*,[5] referred to as BMR in this section, found a solution to this problem by specifying initial conditions that produce a correlated flow field with turbulent characteristics from specified initial energy spectra. For brevity the details of this procedure are not repeated here. Rather, the equations involved and the case referred to as "iga96" in BMR is presented here.

Initial conditions were produced by specifying initial solenoidal velocity (E_s), and dilatational velocity (E_d), density (E_ρ), and temperature (E_T) spectra. All spectra are tophat and have a constant non-zero contribution to wavenumbers between k=8 and k=16. The amplitude in this range is constant, but differs for the various spectra. For case "iga96" in BMR the amplitude for the various spectra is given in Table 1.

The Fourier coefficients for the solenoidal velocity field can

be determined from the spectra as follows,

$$\begin{bmatrix} \hat{u}_s(k) \\ \hat{v}_s(k) \\ \hat{w}_s(k) \end{bmatrix} = \begin{bmatrix} \frac{\alpha^{ran} k k_2 + \beta^{ran} k_1 k_3}{k k_{12}} \\ \frac{\beta^{ran} k_2 k_3 - \alpha^{ran} k k_1}{k k_{12}} \\ \frac{-\beta^{ran} k_{12}}{k} \end{bmatrix}. \quad (6)$$

$\alpha^{ran} = \sqrt{\frac{E_s(k)}{4\pi k^2}} e^{\mathbf{i}\phi_1} \cos(\phi_3)$ and $\beta^{ran} = \sqrt{\frac{E_s(k)}{4\pi k^2}} e^{\mathbf{i}\phi_2} \sin(\phi_3)$. ϕ_1, ϕ_2, and ϕ_3 are uniformly distributed randomly generated numbers. $\mathbf{i}$ is the complex number $\sqrt{-1}$. k is the magnitude of the wavenumber vector, (k_1, k_2, k_3), and k_{12} is expressed as $\sqrt{k_1^2 + k_2^2}$. If $k_{12} = 0$ then $\hat{u} = \alpha^{ran}$, and $\hat{v} = \beta^{ran}$. The dilatational velocity Fourier coefficients are given by

$$\begin{bmatrix} \hat{u}_d(k) \\ \hat{v}_d(k) \\ \hat{w}_d(k) \end{bmatrix} = \begin{bmatrix} \gamma^{ran} k_1/k \\ \gamma^{ran} k_2/k \\ \gamma^{ran} k_3/k \end{bmatrix}, \quad (7)$$

where $\gamma^{ran} = \sqrt{\frac{E_d(k)}{4\pi k^2}} e^{\mathbf{i}\phi_4}$. ϕ_4 is a uniformly distributed randomly generated number. The density and temperature Fourier coefficients are determined with

$$\begin{aligned} \hat{\rho}(k) &= \sqrt{\frac{E_\rho(k)}{4\pi k^2}} e^{\mathbf{i}\phi_5}, \\ \hat{T}(k) &= \sqrt{\frac{E_T(k)}{4\pi k^2}} e^{\mathbf{i}\phi_6}, \end{aligned} \quad (8)$$

where ϕ_4, and ϕ_6 are again uniformly distributed randomly generated numbers.

The initial data is defined on the equi-distant grid with coordinates, $x_i = (l_i - 1)L_f/N, \quad l_i = 1, ..., N$, and wavenumbers, $k_i = \frac{2\pi n_i}{L_f}, \quad n_i = -N/2 + 1, ..., N/2$, in each direction, i=1,2,3. Choosing the reference length, L_f=2π, a three-dimensional discrete Fourier transform can be assembled from the coefficients in (6), (7), and (8). to deteremine the flow field for u, v, w, ρ, and T at the equidistant Fourier grid. The resulting flow field is correlated according to the tophat spectrum.

CMSM employs a Chebyshev grid for simulations. The initial flow field at these points is obtained by performing an eighth-order Lagrangian interpolation on the Fourier grid. To verify whether this interpolation provided sufficient accuracy, the initial flow field was interpolated back to the Fourier grid using spectral interpolation within each element. The energy spectra were determined by applying a Fourier transform on the interpolated values. These spectra were compared to the spectra obtained with the original Fourier expansion.

Figure 1 compares the spectra for a N=64 Fourier expansion and a CMSM grid with 6 equi-distant domains in each direction and approximation orders of $\wp$=9 and 13 on a linear scale (Fig. 1a) and a log scale (Fig. 1b). From Figure 1a it follows that interpolation leads to a 2% underestimation of the amplitude between k=8 and 16 compared to the original Fourier expansion for both approximation orders in CMSM. Both polynomial approximation orders show the same accuracy, which indicates that the difference with the original Fourier expansion is in a large part caused by the eighth-order interpolation to the nonuniform grid.

In the range for $k < 8$ and $k > 16$, the log scale shows that $\wp$=13 is two orders of magnitude closer to the expected value of zero than $\wp$=9. These two orders of magnitude reduction are not conform spectral convergence, but it is expected that the error in this region is limited by the eight-order interpolation from the Fourier grid to the Chebyshev grid. The Fourier expansion clearly has better performance than $\wp$=13 by approximating the spectrum 9 orders of magnitude closer to zero. We are, however, not concerned with this difference, since in comparison to the amplitude of the spectrum of 3.125×10^{-4}, the values outside the interval are negligible in all cases.

Simulations

Simulations are performed on a domain with length 2π and with periodic boundary conditions in each direction. The computational domain is divided into six equi-extent domains in each direction. Two polynomial orders, $\wp$=9 and 13, have been tested. The initial conditions are set as described above. The average initial temperature is $\overline{T}_o$=1.0, which leads to an initial fluctuation Mach number, Ma_0=0.05. Ma_0 is defined as,

$$Ma_0 = \sqrt{u_i'' u_i''}/c(\overline{T}_0), \quad (9)$$

which is written in index notation. The double prime indicates a fluctuating Favre variable. $c(\overline{T})$ is the speed of sound based on the average temperature. The computational Reynolds number, Re_f is set to 2357.

The results, obtained by integrating from the initial flow state, are compared to BMR, who used a N=96 Fourier spectral method. Figure 2 compares the turbulence kinetic energy (TKE), $TKE = 1/2\overline{u_i'' u_i''}$, versus time for the three cases. It is observed that the TKEs are in good agreement for all three cases. The TKE shows the well-known exponential decay[10] in time, which is due to dissipation. The wavy pattern of TKE is a result of the exchange between the kinetic energy and the internal acoustic energy, also known as pressure-dilatation.[11] The good prediction of TKE even by the low order CMSM is surprising, but as mentioned in Ref. 2 TKE is generally predicted well, even by lower order methods.

A better measure of CMSM's performance is given by comparing the evolution of the dissipation rate, ϵ, with time. In compressible turbulence, the solenoidal, ϵ_s, and dilatational, ϵ_d, are the two major contributors to the total dissipation, ϵ. Other higher order contributions turn out to be zero for homogeneous turbulence. Thus, ϵ may be expressed as the

sum of ϵ_s and ϵ_d,

$$\epsilon = \underbrace{\frac{1}{Re_f}\overline{\omega_i'\omega_i'}}_{\epsilon_s} + \underbrace{\frac{4}{3}\frac{1}{Re_f}\overline{\frac{\partial u_i''}{\partial x_i}\frac{\partial u_j''}{\partial x_j}}}_{\epsilon_d}, \quad (10)$$

where ω_i' is the fluid vorticity fluctuation. Figure 3 shows that the results for $\wp$=9 clearly underpredicts ϵ over the entire simulation time as compared to BMR. The results for $\wp$=13, however, indicate good comparison. Inspection of the ϵ_s and ϵ_d contributions to ϵ shows, that the main difference between the two CMSM cases is in the prediction of ϵ_d. The simulation with $\wp$=9 is not able to capture acoustic waves with high frequency, which leads to an underestimation of ϵ_d. Increasing the approximation order to $\wp$=13 leads to a significant increase of the dilatational dissipation, while ϵ_s decreases slightly. Since ϵ agrees well with BMR, it is assumed that the flow is resolved well enough. Figure 4 confirms that $\wp$=9 does not capture the acoustic waves well, since both the pressure variance, $\overline{p'p'}/(\gamma^2\overline{p}^2)$, and the density variance $\overline{\rho'\rho'}/(\overline{\rho}^2)$, are underestimated over the whole time interval. The case with $\wp$=13 again performs far better, and approximates BMR's solution well.

Figure 5 shows the energy spectra for both CMSM cases at t=3.0 and 7.5. Unfortunately, no data for BMR's case is available for comparison. The figure shows that the energy spectra are similar for wave numbers up to $k \sim 16$. Since TKE is half the integrated area under the $E(k)$ curve, and since the magnitude of this integral is mainly determined by the contribution of $E(k)$ up to k=16, the similarity of the spectra explains the similarity of the TKE trend for $\wp$=9 and 13 in Fig. 2. At higher wave numbers, the case with $\wp$=13 shows increased energy compared to $\wp$=9. Since ϵ may alternatively be computed by integrating the area under the curve $k^2E(k)$, also known as the dissipation spectrum, and since $E(k)$ at high k contributes significantly to the integral due to the k^2 term, the increased amplitude in the energy spectrum for $k > 16$ explains the difference in ϵ. Computing ϵ from the dissipation spectrum offers a means to study resolution by inspecting the energy spectrum at large k. If the spectrum shows a sharp drop off at large k this indicates that most dissipation is captured, as the contribution of $E(k)$ in the dissipation spectrum will be small. Memory limitations restrict the computation of the spectrum to k=30, but $E(k)$ clearly shows a sharp drop up to k=30 for $\wp$=13, whereas $\wp$=9 flattens out at higher wave numbers.

An interesting feature of the spectrum is that, unlike what one would expect, the spectrum does not fill out at low wave numbers. In BMR this was explained through the association of vorticity with the solenoidal velocity field, and the acoustic mode with the dilatational velocity field: Vorticity has both a mechanism for generating large scales through vortex stretching and smaller length scales through vortex merging. The solenoidal spectrum thus fills out at both low and high wavenumbers. The acoustic mode, however, has only a mechanism for filling out the high wave number dilatation spectrum through nonlinear steepening of acoustic waves. In this particular computation, it is clear from the dissipation spectrum, that dilatation dominates and determines the spectrum at $k > 16$ for a large part, thus explaining the relatively small filling of the spectrum at low wavenumbers.

In order to verify the spectrum, TKE is computed with $E(k)$ as explained above and compared with the direct computation of TKE for $\wp$=13. Figure 6 shows, that the TKE computed from the spectrum is slightly smaller than the TKE computed directly. The difference, however, is small and attributed to the cutoff of $E(k)$ at k=30. The good comparison of the TKEs indicates a correct energy spectrum trend.

In conclusion $\wp$=13 resolves the flow significantly better than $\wp$=9. $\wp$=13 compares well with BMR, who used a Fourier spectral method with N=96. The good drop off in the energy spectrum at k=30 suggests that at $\wp$=13, 90 Lobatto points (6 domains times 15 Lobatto points) resolve the flow, i.e. 90/30=3 points per wavenumber.

Channel Flow

This section presents results on the compressible flow between parallel plates, also known as channel flow. For incompressible flow, the Navier-Stokes simulations (without models) have been quite extensive. Some of the key works include Kim *et al.*,[12] who performed DNS of the fully turbulent flow at Re_f=3300. They found excellent comparison of the mean flow and first order moments with experimental data and theoretical models, such as the "universal law of the wall." Jimenez and Moin[13] investigated the minimal computational domain necessary to sustain turbulence in the channel flow. They observed longitudinal vortex structures, which they related to the so-called high-speed streaks near the wall. Moser *et al.*[6] performed studies at higher Reynolds number including simulations at the Reynolds number based on the skin friction velocity of Re_τ=200, 500, and 700. In Ref. 14 a resolution study with a spectral element method was employed on the configuration in Ref. 13.

The DNS on compressible channel flow was initiated by Huang *et al.*[15] They performed DNS on the supersonic channel flow at two different Reynolds numbers and found that compressibility effects are limited to inertial effects, which are small. Recently some studies have appeared in literature for subsonic flow, which were mainly used for code or model verification, e.g. Gamet *et al.*[16] and Lenormand *et al.*[17]

In this section, the subsonic compressible channel flow is simulated at a Reynolds number of Re_f=3000 based on the channel half width, L_f, and the average velocity in the channel, u_b. The Mach number Ma_f is chosen to be 0.4 and it is based on the bulk velocity u_b, and the wall temperature

T_{wall}. The purpose of the simulation is to validate and to asses resolution requirements for simulations with CMSM in an inhomogeneous turbulent flow.

Computational Model

Our simulations follow the computational model outlined in Ref. 14 for the DNS of the incompressible channel flow with a spectral element method. The geometry is represented by a rectangle with non-dimensional lengths, L_x=2, L_y=2, and L_z=4 in the wall normal, spanwise, and streamwise directions, respectively. In Ref. 14 a grid of 12 elements in the wall normal direction, 10 elements in the spanwise periodic direction, and a N=64 Fourier expansion in the streamwise periodic direction, was employed. In Ref. 14 the element distribution in the wall normal direction is of a cosine form to account for the higher flow gradients near the wall. In the periodic directions a uniform grid is employed. In the simulation presented here the same element distribution is employed. However, CMSM is used for the approximation in the streamwise direction as opposed to the Fourier spectral method in Ref. 14. Based upon simulations in the previous section on the isotropic turbulence, a 10 domain grid distribution was chosen for simulation with CMSM to obtain a resolution similar to the Fourier grid resolution in Ref. 14. To achieve a resolved flow it was shown in Ref. 14 that a polynomial approximation of $\wp$=10 is sufficient. This section presents results for $\wp$=6 and 10.

Periodicity in the streamwise direction is not trivial, since in the channel flow a negative pressure gradient sustains the flow, which means a non-periodic inhomogeneity. It can be shown by integration of the Navier-Stokes equations over the width of the channel, that specifying a constant source term leads to a mass flux that is time-dependent (Lenormand *et al.*[17]). This makes the analysis of the flow at a constant Reynolds number impossible. In order for the mass flux to be time-independent, it was shown that the forcing term has to be time dependent. The algorithm presented in Ref. 17 for maintaining a constant mass force is employed here as well. The wall boundary condition is set as isothermal.

Initiation and Transition to Turbulence

The velocity field is initialized with the laminar parabolic Poiseuille profile with a random disturbance in the streamwise velocity, as,

$$u(y) = -6\left[\left(\frac{y}{2}\right)^2 - \frac{y}{2}\right](1+\epsilon), \qquad (11)$$

where ϵ is a 10% random disturbance. The random disturbance is introduced to accelerate the transition to a turbulent flow. For the temperature, the laminar Poiseuille profile is initially specified as,

$$T(y) = T_{wall} + \left\{\frac{3(\gamma-1)}{4Pr}\left[1-(y-1)^4\right]\right\}, \qquad (12)$$

where T_{wall} is the wall temperature. The density is initially set constant. The pressure follows from the constant density, the initial temperature and the ideal gas law.

With this initial flow field and the resolution described in the previous section, the initial disturbance damps out at the intended Reynolds number of Re_f=3000 and the flow returns to its laminar state. Increasing the Reynolds number to Re_f=6000 to force transition does not lead to transition within computational times that are feasible. Rather than increasing the Reynolds number even more, the flow is simulated at a lower resolution of $\wp$=2 in the hope that truncation error of the scheme acts as a sufficiently large disturbance required for transition. From Fig. 7, which shows the average skin friction coefficient, c_f, plotted versus time, it is observed that this approach works: Up to time, $t \sim$20 the flow maintains its laminar skin friction coefficient of $c_f = 3/Re_f$=0.001, but for times $t >$20, c_f increases indicating transition. At time $t \sim$80, c_f levels off at the expected turbulent c_f of approximately 0.042. Through interpolation of the solution at $\wp$=2 at four times two incrementals of $\wp$ and consequently simulating for short times, a turbulent initial condition for the simulation at $\wp$=10 is specified. Results of the quasi-steady state channel flow obtained by simulating from this initial condition are presented in the next section.

Simulations

The results of the simulations are presented for $\wp$=6, and $\wp$=10 and are compared to the results of Moser *et al.* 1999 (MKM).

Instantaneous flow field

Figure 8 shows the u-velocity contours close to the wall at z=0.01. Clearly visible is the streaky pattern observed in other works (e.g. Refs. 10,12,13) that is caused by the long vorticial structures. Three high speed and low speed streaks may be observed. An approximate separation of the streaks is 0.33 in y-direction, which is computed as the ratio of the two length units width of the computational domain over the six number of streaks. This separation is in good agreement with Ref. 12, where the separation was reported to be 0.3. In Fig. 9, the longitudinal vortices are visualized by temperature iso-contours colored with the u-velocity. The distance between these two long vortices is approximately 0.5 in y-direction, again showing a good agreement with the reported value of 0.5 in Ref. 12.

Comparison of average flow field

The Favre averaged velocity scaled with the skin friction velocity, u^+, plotted versus the wall normal coordinate, z, for

$\wp$=6 and $\wp$=10 is shown in Fig. 10a. Here, the skin friction velocity, u_τ, is defined as

$$u_\tau = \sqrt{\frac{\tau_{wall}}{\rho_{wall}}}, \tag{13}$$

where τ_{wall} and ρ_{wall} are the average shear stress and density at the wall, respectively. It is observed that increasing the polynomial order leads to a closer agreement with MKM's results. At $\wp$=6 the skin friction velocity is underpredicted. Furthermore, the solution is slightly asymmetric due to the upwinding properties of the Roe solver. At $\wp$=10 the solution shows increased symmetry. The skin friction velocity, u_τ, is 0.062, within 3% agreement of Dean's correlation[18] of 0.064. In Fig. 10b, the same velocity u^+ is plotted versus the wall coordinate z^+, defined as,

$$z^+ = \rho_{wall} z u_\tau Re_f \tag{14}$$

It is observed that $\wp$=6 slightly overpredicts the average velocity, but $\wp$=10 is in excellent agreement with MKM's results and the theoretical "law of the wall[10]" given by,

$$\begin{aligned} u^+ &= z^+ & z^+ < 10 \\ u^+ &= 2.5 \ln z^+ + 5.5 & z^+ > 10 \end{aligned} \tag{15}$$

Figure 10c compares the averaged spanwise v velocity scaled with u_τ, v^+, plotted versus the wall normal coordinate for $\wp$=6 and 10 with MKM's result. At the symmetry line the v^+ velocity of MKM is not zero, whereas symmetry considerations suggest a zero v^+ velocity. In MKM this discrepancy was claimed to be an indication of the accuracy of the computation. The error is on the order of 1% of the average u^+. CMSM predicts a symmetry v^+ slightly closer to the zero symmetry value than MKM result. The trend of v^+, however, shows differences with MKM, which most likely result from the different approximation in streamwise direction through CMSM here versus the Fourier spectral method in MKM. Increasing $\wp$ from 6 to 10 decreases the peak values of v^+ from 2% to 1% of the average u^+ velocity.

Figure 10d shows the averaged density, $\overline{\rho}$, for both polynomial orders. Since MKM's simulations are incompressible no comparison with MKM is available. It is observed that there is approximately a 2.3% increase in density near the wall for Ma_f=0.4, indicating a relatively small effect of compressibility. Increasing $\wp$ from 6 to 10 leads to less than 0.02% difference in the density distribution.

Comparison of turbulence statistics

Figure 11 shows that the Favre fluctuating root mean square velocity components, normalized with u_τ, compare well for $\wp$=10 with the results presented in MKM. At $\wp$=6 the main discrepancy is in the peak value of u''^+_{rms}. However, the trends for the various rms components are comparable. A similar conclusion may be drawn for the off-diagonal Reynolds stress component $\widetilde{u''w''}^+$ for $\wp$=6 presented in Fig. 12, which shows an overprediction of its peak value close to the wall as compared to MKM. It is observed that the overpredicted $\widetilde{u''w''}^+$ near the wall is compensated for further away from the wall, where $\widetilde{u''w''}^+$ is underpredicted. This discrepancy seems to be related to the positive values of $\widetilde{u''v''}^+$, which should theoretically be zero. The positive $\widetilde{u''v''}^+$ is in turn most likely related to the aforementioned asymmetry in the u-velocity profile. At $\wp$=10, the asymmetry is far less, but the $\widetilde{u''w''}^+$ Reynolds stress component is still larger than the result predicted by MKM. However, for $\wp$=10 no compensation further away from the wall is observed like for $\wp$=6. Furthermore, $\widetilde{u''v''}^+$ is much closer to its theoretical zero value than for $\wp$=6. Results from incompressible DNS simulations in Ref. 12 and experimental measurements in Ref. 19 indicate that $\widetilde{u''v''}^+$ may be larger than that predicted by MKM: for example, Ref. 19 predicts peak values of $\widetilde{u''v''}^+ = -0.78$, which is comparable to the peak value of -0.79 predicted by CMSM.

Finally, as a good measure of the resolution in Fig. 13, we plot the solenoidal part of the dissipation (10) normalized with u_τ. It is noted that the dilatational terms and terms that appear due to inhomogeneity in the dissipation rate do not exceed 1% of the peak value of the solenoidal dissipation, confirming the relative small influence of dilatation on the compressible channel flow. As in the isotropic turbulence, the lower order polynomial underpredicts dissipation, whereas the result for $\wp$=10 underpredicts the dissipation less. Furthermore at $\wp$=10, the trends are the same, and the skin friction is expected to be lower due to the increased density near the wall. The main difference between $\wp$=6 and $\wp$=10 is found near the wall where $\wp$=6 is not able to capture the high velocity gradient in the viscous sublayer as well as $\wp$=10.

Assessment of resolution

In conclusion, the results at $\wp$=10 compare well to MKM's results and expected channel behavior. MKM reported good drop off in the one-dimensional streamwise and spanwise spectra at wavenumbers k_x=30 and k_y=90, respectively. The stream and spanwise dimensions of the computational domain in our simulation are L_x=4 an L_y=2, i.e. the number of waves at the drop off wave numbers in our domain are $L_x k_x/2\pi$=19 and $L_y k_y/2\pi$=28. In both directions 120 Lobatto points are used to resolve the flow. Thus a resolution of 6 and 4 points per wavenumber (ratio of the number of waves in the domain over the number of Lobatto points) sufficiently resolves the flow in stream and spanwise direction.

Conclusions

To initiate the DNS study of three-dimensional compressible

turbulent flows with multidomain spectral methods, simulations are conducted in the setting of an isotropic decaying turbulence for purposes of code validation and assessment of resolution requirements. The initial conditions are determined on a Fourier grid in the wave space, and the physical flow field is determined through a Fourier transform. The physical flow field interpolated to the Chebyshev grid with an eighth-order Lagrangian interpolation scheme provides an accurate initial turbulence. Six domains with a polynomial order approximation, $\wp$=13, in each direction resolves the flow comparably well to a Fourier spectral method, with N=96.

For further validation of the code and assessment of resolution requirements for CMSM in inhomogeneous turbulence, a fully turbulent channel flow simulation is performed at Reynolds and Mach numbers of $Re_f = 3000$ and $Ma_f = 0.4$, respectively, based on the channel half width, the bulk velocity and the wall temperature. Transition to turbulence from the laminar initial state is obtained by simulating at low resolution, such that the round off errors of the scheme introduced the flow disturbances required for transition. By interpolating the result to a grid with a higher order polynomial and continuing the simulation, the resolved resolution result is obtained. If the high resolution is employed from the initial time, transition from the laminar initial state does not occur within feasible computational times for Reynolds numbers up to $Re_f = 6000$. Comparison of the turbulent statistics shows excellent agreement with previously published results. Compressibility effects at this Mach number are limited to a 2% increase in the averaged density near the wall and a maximum 1% contribution of the non-solenoidal dissipation terms to the total dissipation.

Acknowledgment

The support for this work was provided by the U.S. Office of Naval Research under Grant N00014-99-1-0808 with Dr. G.D. Roy as Technical Monitor, and by the National Science Foundation under Grant CTS-0237951 with Dr. T.J. Mountziaris as Program Director, and by the FSU School for Computational Science and Information Technology (CSIT), by a grant of resources on the IBM pSeries 690 Power4-based supercomputer "Eclipse".

References

[1] Kopriva, D. A., "A Staggered-Grid Multidomain Spectral Method for the Compressible Navier-Stokes Equations," *J. Comp. Phys.*, Vol. 244, 1998, pp. 142–158.

[2] Moin, P. and Mahesh, K., "Direct Numerical Simulation: A Tool in Turbulence Research," *Ann. Rev. Fluid Mech.*, Vol. 30, 1998, pp. 539–578.

[3] Jacobs, G. B., Kopriva, D. A., and Mashayek, F., "A comparison of outflow boundary conditions for the multidomain staggered-grid spectral method," *Num. Heat Transfer, Part B*, Vol. 44, 2003, pp. 225–251.

[4] Jacobs, G. B., Kopriva, D. A., and Mashayek, F., "Compressibility effects on the subsonic two-phase flow over a square cylinder," *J. Propulsion and Power*, 2003. To appear.

[5] Blaisdell, G. A., Mansour, N. N., and Reynolds, W. C., "Compressibility Effects on the Growth and Structure of Homogeneous Turbulent Shear Flow," *J. Fluid Mech.*, Vol. 256, 1993, pp. 443–485.

[6] Moser, R., Kim, J., and Mansour, N. N., "Direct numerical simulation of turbulent channel flow up to Re_τ=590," *Phys. Fluids*, Vol. 11, Apr. 1999, pp. 943–945.

[7] Kopriva, D. A. and Kolias, J. H., "A Conservative Staggered-Grid Chebyshev Multidomain Method for Compressible Flows," *J. Comp. Phys.*, Vol. 125, 1996, pp. 244–261.

[8] Roe, P. L., "Approximate Riemann Solvers, Parameter Vectors, and Difference Schemes," *J. Comp. Phys.*, Vol. 43, 1981, pp. 357–372.

[9] Rogallo, R. S., "Numerical Experiments in Homogeneous Turbulence," NASA TM 81315, 1981.

[10] Nieuwstadt, F. T. M., *Turbulentie, inleiding in de theorie en toepassing van turbulente stromingen.* Utrecht, The Netherlands: Epsilon Uitgaven, 1992.

[11] Kida, S. and Orszag, S., "Energy and Spectral Dynamics in Decaying Compressible Turbulence," *Journal of Scientific Computing*, Vol. 7, No. 1, 1992, pp. 1–34.

[12] Kim, J., Moin, P., and Moser, R. D., "Turbulent Statistics in Fully Developed Turbulent Channel Flow at Low Reynolds Number," *J. Fluid Mech.*, Vol. 177, 1987, pp. 133–166.

[13] Jimenez, J. and Moin, P., "The Minimal Flow Unit in Near-Wall Turbulence," *J. Fluid Mech.*, Vol. 225, 1991, pp. 213–240.

[14] Karniadakis, G. E. and Sherwin, S. J., *Spectral/hp Element Methods for CFD.* New York, NY: Oxford University Press, 1999.

[15] Huang, P. G., Coleman, G., and Bradshaw, P., "Compressible Turbulent Channel Flows: DNS results and modelling," *J. Fluid Mech.*, Vol. 305, 1995, pp. 185–218.

Spectrum	Initial value
$E_s(k)$	2.8125×10^{-4}
$E_d(k)$	3.1250×10^{-5}
$E_\rho(k)$	1.2500×10^{-3}
$E_T(k)$	1.2500×10^{-3}

Table 1: Initial values of the various spectra for case "iga96" from isotropic decaying turbulence simulations from BMR.

[16] Gamet, L., Ducros, F., Nicoud, F., and Poinsot, T., "Compact finite difference schemes on non-uniform meshs. Application to direct numercial simulations of compressible flows.," *Int. J. Numer. Meth. Fluids*, Vol. 29, 1999, pp. 159–191.

[17] Lenormand, E., Sagaut, P., and Ta Phuoc, L., "Large eddy simulation of subsonic and supersonic channel flow at moderate Reynolds number," *Int. J. Numer. Meth. Fluids*, Vol. 32, 2000, pp. 369–406.

[18] Dean, R., "Reynolds number dependence of skin friction and other bulk flow variables in two-dimensional rectangular duct flow," *J. Fluids Eng.*, Vol. 215, 1978, pp. 215–223.

[19] Niederschulte, M. A., Adrian, R. J., and Hanratty, T., "Measurements of turbulent flow in a channel flow at low Reynolds numbers," *Exp. Fluids*, Vol. 9, 1990, pp. 222–230.

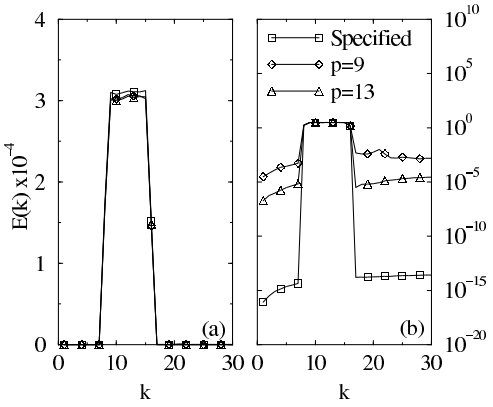

Figure 1: Comparison of the initial energy spectrum in isotropic turbulence for BMR, and CMSM, $\wp$=9 and $\wp$=13 on a linear (a), and a log (b) scale.

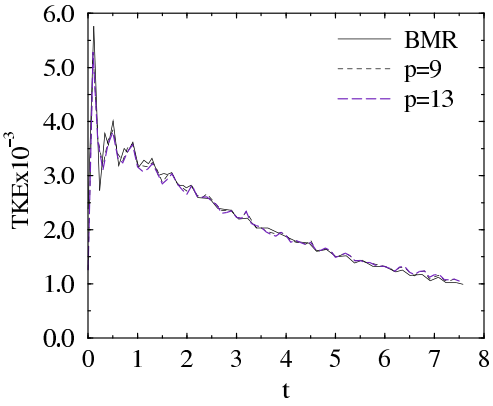

Figure 2: Comparison of the turbulence kinetic energy (TKE) versus time, t, in isotropic turbulence for BMR and CMSM, $\wp$=9 and $\wp$=13.

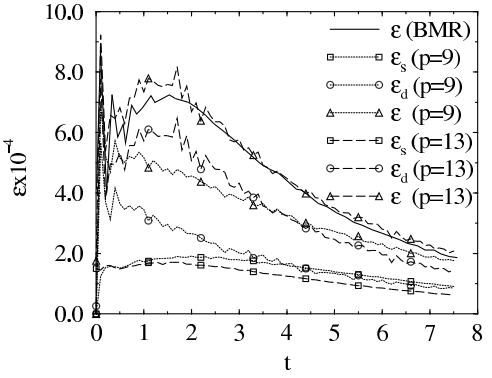

Figure 3: Comparison of the turbulence dissipation rate, ϵ, versus time, t, in isotropic turbulence for BMR and CMSM, with $\wp$=9 and $\wp$=13. For CMSM the contributions of both the solenoidal, ϵ_s, and dilatational, ϵ_d, dissipation rates are also shown.

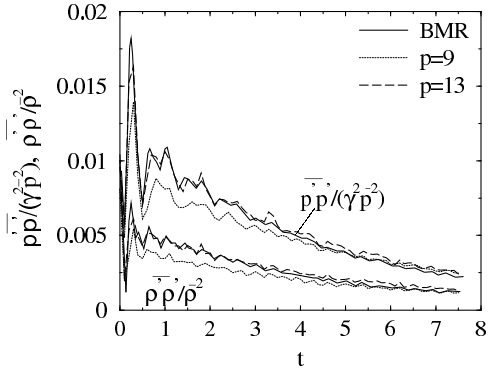

Figure 4: Comparison of the pressure variance, $\overline{p'p'}/(\gamma^2\overline{p}^2)$, and the density variance, $\overline{\rho'\rho'}/(\overline{\rho}^2)$, versus time, t, in isotropic turbulence for BMR and CMSM, $\wp$=9 and $\wp$=13.

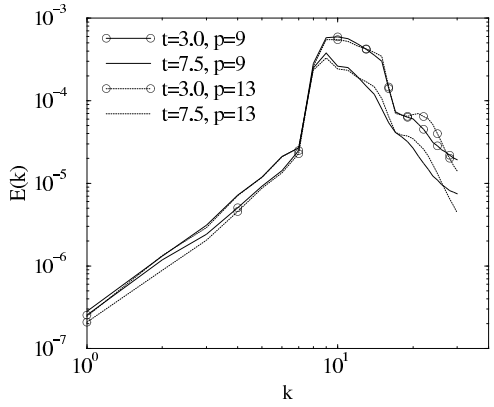

Figure 5: Comparison of the energy spectra, $E(k)$, versus the wave number, k, at t=3.0 and 7.5 for CMSM with $\wp$=9 and $\wp$=13 in isotropic turbulence.

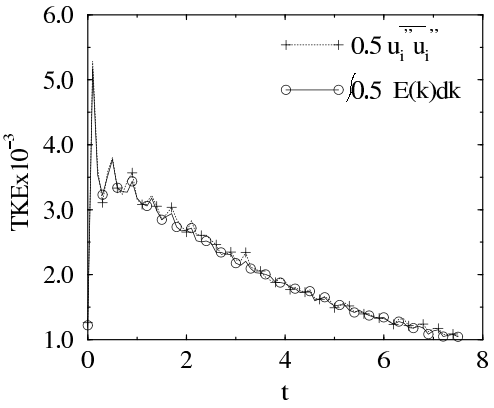

Figure 6: Comparison of the turbulent kinetic energy (TKE) versus time, t, in isotropic turbulence computed with $0.5\overline{u_i'' u_i''}$, and $0.5\int_0^\infty E(k)dk$ for $\wp$=13.

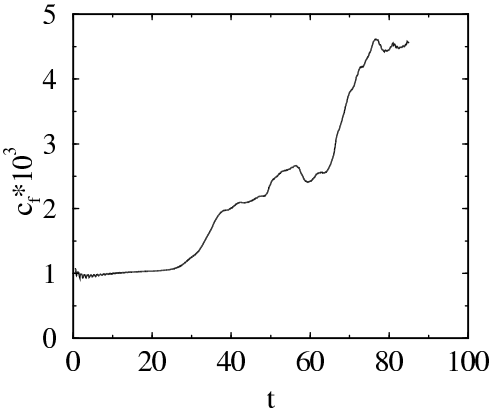

Figure 7: Skin friction coefficient, c_f, plotted versus time, t, showing transition to turbulence in a channel flow.

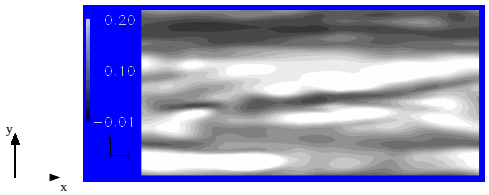

Figure 8: Instantaneous streamwise u velocity contour at z=0.01 in a channel flow for $\wp$=10.

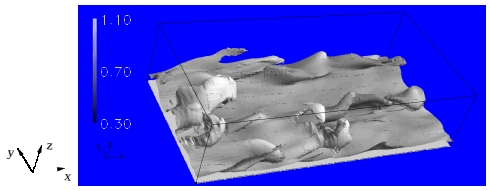

Figure 9: Instantaneous temperature iso-contours in a channel flow colored with the streamwise u velocity component for $\wp$=10.

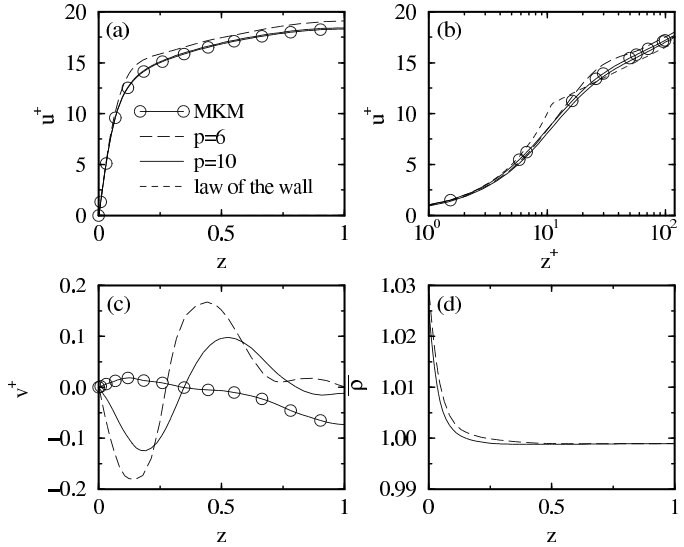

Figure 10: Various averaged flow variables in the channel flow plotted in wall normal direction: u^+ plotted versus z (a), and z^+ (b). v^+ plotted versus z (c). $\overline{\rho}$ plotted versus z (d).

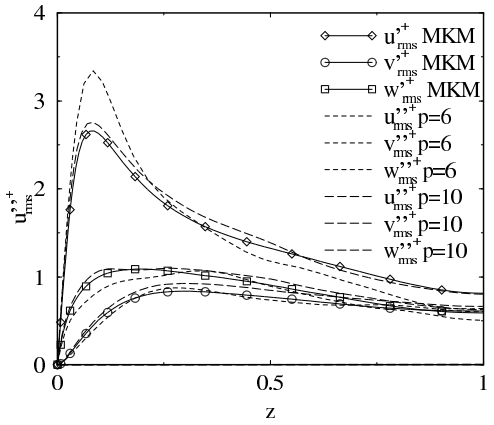

Figure 11: Root mean square Favre fluctuation velocities normalized with u_τ, u''^+_{rms}, v''^+_{rms} and w''^+_{rms} for $\wp$=6 and $\wp$=10, compared with the Reynolds fluctuating velocities normalized with u_τ, u'^+_{rms}, v'^+_{rms} and w'^+_{rms} from MKM plotted versus z in the channel flow.

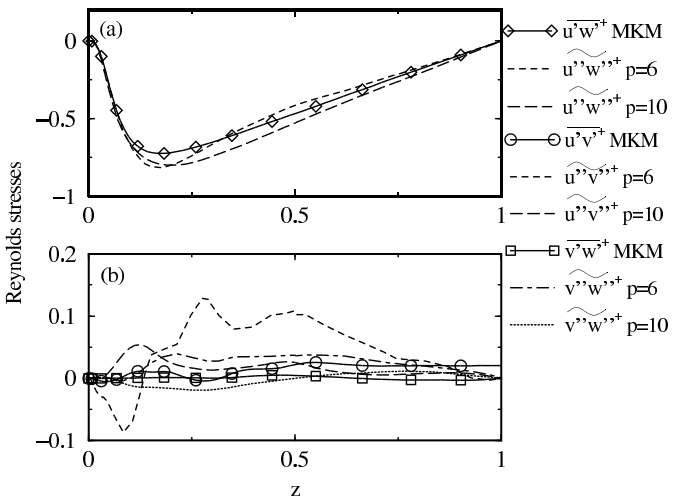

Figure 12: Favre averaged Reynolds stresses normalized with u_τ, $\widetilde{u''w''}^+$ (a) , $\widetilde{u''v''}^+$ (b) and $\widetilde{v''w''}^+$(b) compared with the Reynolds averaged Reynolds stresses normalized with u_τ, $\overline{u'w'}^+$ (a), $\overline{u'v'}^+$ (b) and $\overline{v'w'}^+$ (b) from MKM plotted versus z in the channel flow.

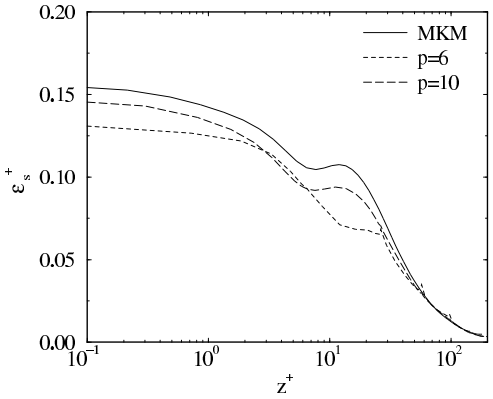

Figure 13: Reynolds averaged solenoidal dissipation rate, $\epsilon_s^+ = \frac{1}{Re_f}\overline{\omega_i'\omega_i'}^+$ for $\wp$=6 and $\wp$=10 compared with MKM plotted versus z^+.